Energy Materials and Devices

Open Access
Research Article

Graphical Abstract

Trace ruthenium enables synergistic interactions in NiFeB nanosheets for industrial-current-density water oxidation

Shiyu Chen[1], Yang Li[1], Chunling Lu[1], Biao Wang[1], Junru Jiang[1], Dongchao Qiu[1], Bingbing Niu[1,2] ✉, and Tao Feng[3] ✉

[1] *School of Science, University of Science and Technology Liaoning, Anshan 114051, China*
[2] *Key Laboratory of Interfacial Physics and Technology, Shanghai Institute of Applied Physics, Chinese Academy of Sciences, Shanghai 201800, China*
[3] *Department of Materials Science and Engineering, Southern University of Science and Technology, Shenzhen 518055, China*

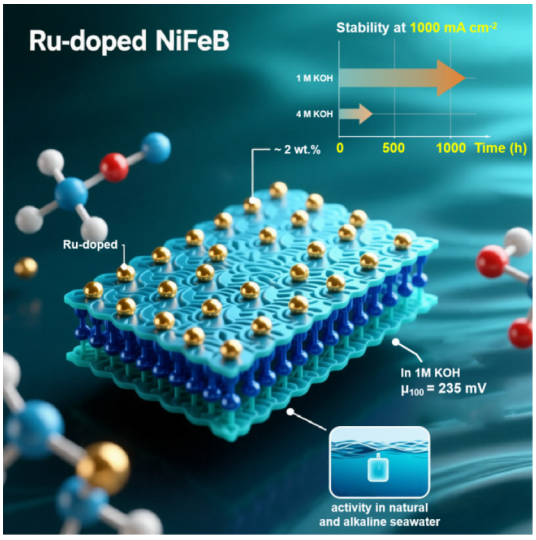

This study reports the successful construction of a hierarchical Ru-doped NiFeB nanosheet electrocatalyst (Ru@NiFeB) via a scalable synthesis approach. The catalyst exhibits outstanding oxygen evolution reaction activity and exceptional operational stability at industrial current densities, which are attributed to the precise modulation of the electronic structure by trace Ru dopants and the optimization of adsorption energetics for oxygen intermediates. The electrode also demonstrates remarkable full-cell performance and long-term durability in both concentrated alkaline and seawater electrolytes, thereby offering an efficient and robust anode solution for large-scale green hydrogen production.

✉Address correspondence to **Bingbing Niu**, niubb92@foxmail.com; **Tao Feng**, fengt@sustech.edu.cn

Received: November 17, 2025
Revised: December 30, 2025
Accepted: January 4, 2026

9370085

Read Online

Citation: Chen S., Li Y., Lu C., et al. Trace ruthenium enables synergistic interactions in NiFeB nanosheets for industrial-current-density water oxidation. *Energy Mater. Devices*, 2026, 4(1), 9370085. https://doi.org/10.26599/EMD.2026.9370085

Energy Materials and Devices
https://doi.org/10.26599/EMD.2026.9370085
Open Access
Research Article

Trace ruthenium enables synergistic interactions in NiFeB nanosheets for industrial-current-density water oxidation

Shiyu Chen[1], Yang Li[1], Chunling Lu[1], Biao Wang[1], Junru Jiang[1], Dongchao Qiu[1], Bingbing Niu[1,2] ✉, and Tao Feng[3] ✉

[1] *School of Science, University of Science and Technology Liaoning, Anshan 114051, China*
[2] *Key Laboratory of Interfacial Physics and Technology, Shanghai Institute of Applied Physics, Chinese Academy of Sciences, Shanghai 201800, China*
[3] *Department of Materials Science and Engineering, Southern University of Science and Technology, Shenzhen 518055, China*

Cite this article: *Energy Mater. Devices* 2026, **4**(1): 9370085. https://doi.org/10.26599/EMD.2026.9370085

ABSTRACT

The oxygen evolution reaction (OER) represents the dominant kinetic bottleneck in electrochemical water splitting, thereby imposing stringent demands on the development of advanced electrocatalysts that simultaneously deliver high activity and long-term stability under industrial operating conditions for large-scale hydrogen production. Here, we report the rational design and fabrication of a hierarchical Ru-decorated NiFeB nanosheet architecture (Ru@NiFeB), constructed via sequential electrodeposition and hydrothermal processing on three-dimensional nickel foam substrate. The strategic incorporation of trace Ru species (~2 wt.%) drives pronounced electronic modulation at the heterointerface, thereby fundamentally regulating the adsorption energetics of oxygen-containing intermediates. The resulting Ru@NiFeB electrode exhibits state-of-the-art OER performance, with an overpotential of merely 235 mV at 100 mA/cm^2 in 1 mol/L KOH, surpassing the activity of commercial RuO_2 catalysts. Remarkably, the electrode sustains a current density of 1000 mA/cm^2 for over 150 h in a concentrated 4 mol/L KOH electrolyte without discernible degradation, thereby establishing one of the most stable low-doped noble metal-based OER catalysts reported to date. This work establishes a viable pathway toward cost-effective and robust electrocatalysts for industrial alkaline water electrolysis, thereby substantially advancing the feasibility of large-scale green hydrogen production.

KEYWORDS

electrocatalyst, ruthenium doping, oxygen evolution reaction, high current density.

1 Introduction

Electrocatalytic water splitting is widely regarded as a promising strategy for sustainable hydrogen production that enables efficient utilization of intermittent renewable energy sources[1]. The oxygen evolution reaction (OER) involves a complex four-electron transfer process, which remains the primary kinetic bottleneck in overall water splitting[2,3]. While noble metal-based catalysts (RuO_2 and IrO_2) demonstrate superior catalytic activity, their prohibitive cost and limited natural abundance preclude widespread large-scale industrial deployment[4]. Consequently, the development of earth-abundant transition-metal-based electrocatalysts with performance comparable to noble-metal catalysts has emerged as a critical research priority[5].

Nickel (Ni) and iron (Fe)-based materials have attracted considerable interest as promising alternatives owing to their high natural abundance, cost-effectiveness, and favorable electrocatalytic performance in a wide range of electrochemical reactions. Previous studies have revealed a pronounced synergistic effect between Ni and Fe in bimetallic catalytic systems[6,7]. Specifically, the incorporation of Fe^{3+} can induce the preoxidation of Ni^{2+} sites, thereby promoting the formation of higher-valence Ni species (Ni^{3+}/Ni^{4+}), which are widely recognized as the true catalytically active centers in the OER catalytic cycle[8,9]. Furthermore, the introduction of Fe effectively tunes the adsorption energies of oxygen intermediates and lowers the reaction energy barrier, thereby significantly enhancing the intrinsic catalytic activity toward the OER. However, many NiFe-based catalysts still exhibit high overpotentials and insufficient operational durability at industrially relevant current densities (>500 mA/cm^2) [5,10]. For instance, typical NiFe layered double hydroxide catalysts require an overpotential (η) of approximately 230 mV to achieve a current density of 10 mA/cm^2 in 1 mol/L KOH but often degrade rapidly under industrial-grade current densities[11]. To address these limitations, heteroatom doping strategies have emerged as an effective approach

Received: November 17, 2025 / **Revised:** December 30, 2025 / **Accepted:** January 4, 2026

✉**Address correspondence to** Bingbing Niu, niubb92@foxmail.com; Tao Feng, fengt@sustech.edu.cn

for modulating the electronic structure and substantially enhancing the catalytic performance of transition-metal-based compounds[5,11–14].

Among various dopants, boron (B) incorporation offers unique and multifaceted advantages through multiple mechanisms, including the optimization of active-site electronic states, the promotion of oxygen-vacancy formation, the enhancement of electrochemically active surface area (ECSA), and the acceleration of charge-transfer kinetics[15–17]. Recent investigations have demonstrated substantial enhancements in electrocatalytic performance through boron doping. Bai et al. reported that NiFeB layered double hydroxides achieved an overpotential of 290 mV at 100 mA/cm^2 [15]. Aras et al. approximately 21% enhancement in electrocatalytic performance in Mo_2CoB_2 compared to pristine cobalt electrodes[18]. Hua et al. developed Pd–NiFeB catalysts that require only 1.81 V to drive overall water splitting (OWS) at 500 mA/cm^2 [17]. Nevertheless, maintaining structural integrity and catalytic performance under prolonged high current-density operation remains a significant challenge. A promising approach to address this issue is the hierarchical nanostructuring of three-dimensional conductive substrates, which can simultaneously promote mass transport, electrical conductivity, and the accessibility of active sites[19]. Additionally, the strategic incorporation of trace amounts of noble-metal nanoclusters has been shown to synergistically modulate the electronic structure while substantially minimizing the use of precious metals[17].

Herein, we report a scalable and rational multistep synthesis strategy combining electrodeposition, chemical treatment, and hydrothermal processing to construct self-supported Ru-modified nickel–iron–boron nanostructured electrodes (Ru@NiFeB) directly on three-dimensional nickel foam substrates. This binder-free architecture exploits the synergistic effects between the high-surface-area NiFeB matrix and atomically dispersed Ru species to precisely regulate intermediate adsorption energetics. The resulting electrode demonstrates outstanding performance in 4 mol/L KOH, achieving a low voltage of only 2.30 V to sustain a high current density of 1000 mA/cm^2 with excellent stability. Notably, the half-cell exhibits stable operation for over 1200 h at a current density of 1000 mA/cm^2, whereas the full cell maintains stable performance for 150 h at 1000 mA/cm^2 in 4 mol/L KOH. Additionally, the electrode remains highly stable for 200 h at 1000 mA/cm^2 in natural seawater. This work significantly advances the rational design of efficient and stable electrocatalysts for industrial-scale green hydrogen production, demonstrating both high performance and excellent long-term operational stability under diverse electrolytic conditions. The overall synthesis procedure is shown in Scheme 1.

2 Materials and methods

2.1 Materials

All chemicals used were of analytical grade and purchased from Aladdin Scientific. These include nickel sulfate hexahydrate ($NiSO_4·6H_2O$), ferrous sulfate heptahydrate ($FeSO_4·7H_2O$), ruthenium chloride hydrate ($RuCl_3·xH_2O$), sodium borohydride solution ($NaBH_4$), ascorbic acid ($C_6H_8O_6$), hydrochloric acid (HCl), and potassium hydroxide (KOH). Nickel foam (NF) was obtained from Shanghai Jiaqingyuan Co., Ltd. (China). All reagents were used without further purification unless otherwise stated.

2.2 Synthesis of the Ru@NiFeB electrocatalyst

The NiFe-based substrate was synthesized using a three-dimensional porous NF, 1 × 1 cm^2) as the base material. A NiFe layer was electrochemically deposited onto the NF using the following stepwise procedure: A 0.01 mol/L $NiSO_4·6H_2O$ solution and a 0.05 mol/L $FeSO_4·7H_2O$ solution were prepared as the nickel and iron sources, respectively, with a 0.1 mol/L $NaBH_4$ solution serving as the boron source. Electrochemical deposition was performed using a three-electrode electrochemical workstation at −1.1 V for 400 s to form the NiFe template. The electrode configuration consisted of NF as the working electrode, a platinum foil as the counter electrode, and an Ag/AgCl electrode as the reference electrode. After optimizing the parameters of molar concentration, current density, and electrochemical deposition time, NiFe@NF was removed from the deposition solution, washed with deionized water, and dried under ambient conditions. The dried sample was then immersed in a 0.1 mol/L $NaBH_4$ solution and reacted at 80°C for 40 min to complete the prepara-

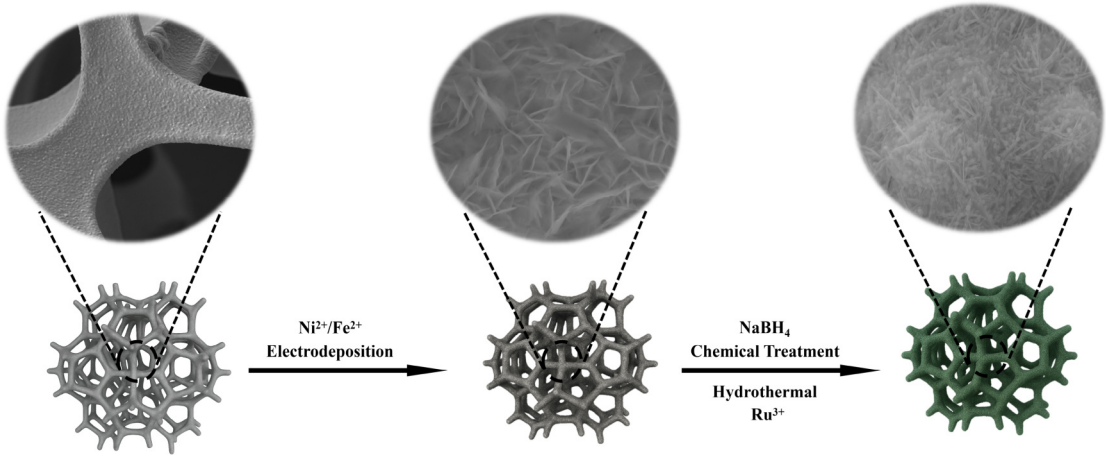

Scheme 1 Synthesis schematic of Ru@NiFeB

tion of the NiFeB substrate.

After synthesizing the NiFeB substrate, Ru doping was performed using a hydrothermal method. The hydrothermal time for Ru deposition was systematically optimized from 40 to 120 min. As shown in Figs. S1–S4 in Supplementary Material, the catalyst deposited for 60 min features a uniform nanosheet architecture, optimizing active site exposure and reactant mass transfer. Electrochemical tests confirm its performance, as it exhibits the lowest overpotential of 238 mV at a current density of 100 mA/cm^2 among various deposition times, reflecting superior intrinsic activity and a minimal Tafel slope of 66.8 mV/dec, which indicates faster reaction kinetics. Furthermore, it has the largest electrochemically active surface area of 9.8 mF/cm^2, aligning with its well-developed morphology. These characteristics ensure efficient and stable performance, making 60 min the optimal deposition time for Ru hydrothermal processes, leading to significantly enhanced oxygen evolution reaction performance with the Ru@NiFeB catalyst. A 0.2 mmol/L Ru precursor ($RuCl_3{\cdot}xH_2O$) was dissolved in 30 mL of deionized water to prepare the doping solution. The solution was then combined with the NiFeB/NF substrate and transferred to a Teflon-lined hydrothermal autoclave. The reaction was conducted at 100°C for 60 min to complete Ru doping. After cooling to room temperature, the Ru@NiFeB catalyst was collected. The Ru doping content was confirmed to be 2.26 wt.% via inductively coupled plasma (ICP) analysis. To optimize the doping process, the reaction time and temperature were systematically adjusted and evaluated. Finally, the doped Ru@NiFeB catalyst was washed with deionized water and dried at 60°C.

2.3 Catalyst characterization

The surface morphology of the catalyst was examined using a field-emission scanning electron microscope (SEM; Zeiss Crossbeam 540). The catalyst was sectioned into 5 mm × 5 mm pieces and mounted onto the sample holder with conductive glue. Further microstructural insights were obtained using a field-emission transmission electron microscope (TEM; FEI Tecnai F20). The crystal structure was analyzed via X-ray diffraction (XRD) using a Bruker D8 Advance system with Cu Kα radiation (wavelength = 1.5406 Å), a current of 40 mA, a voltage of 40 kV, and a scan range of 10°–90° at a scan rate of 5°/min. Raman spectroscopy was performed using an iHR550 Evolution system with a 532 nm laser to probe the local chemical structure of the catalyst. Elemental composition and chemical state analysis were performed using X-ray photoelectron spectroscopy (XPS; ESCALAB Xi+), with a survey area of 15–900 μm and an energy range of 0–1500 eV. Data were calibrated using the C 1s peak at 284.8 eV. Quantitative analysis of metal elements was conducted via ICP optical emission spectroscopy (ICP-OES; Optima 8000), with a spectral range of 130–770 nm and a 27.12 MHz generator.

3 Result and discussion

3.1 Morphology and structural characterizations

The Ru@NiFeB nanosheets were synthesized by precisely controlling the Ru deposition time on the NiFeB substrate, with a hydrothermal reaction at 100°C for 60 min identified as the optimal condition. The surface morphology of the Ru@NiFeB catalyst was observed using field-emission SEM, revealing a fibrous or sheet-like microstructure. This structural feature suggests that the catalyst possesses a high specific surface area, which is beneficial for increasing the density of active sites during catalytic reactions, thereby enhancing its OER performance.

Furthermore, energy dispersive X-ray spectroscopy (EDS) analysis, illustrated in Figs. 1a–1e, confirmed the successful incorporation of Ru into the NiFeB substrate, along with the presence of Ni, Fe, and B. The EDS line-scan profile further verified the uniform distribution of these elements across the catalyst surface. This uniform distribution of Ru, Ni, Fe, and B suggests that Ru has been effectively integrated into the NiFeB structure, which likely contributes to enhanced electronic conductivity, improved reaction kinetics, and superior catalytic stability and overall performance.

High-resolution TEM images reveal the crystal structure of the Ru@NiFeB catalyst, as shown in Fig. 2a. The surface maps further validated the successful existence of Ru, Ni, Fe, and B elements as shown in Figs. S5a–5e in Supplementary Material. High-resolution TEM analysis

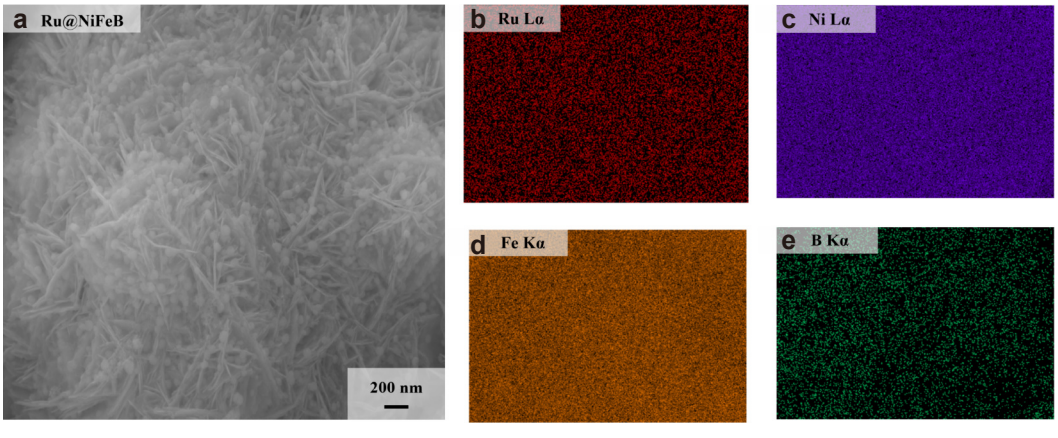

Figure 1 (a) SEM images of Ru@NiFeB. (b)–(e) EDS elemental mapping images of the Ru@NiFeB surface. The corresponding EDS line profiles of Ru Lα (b), Ni Lα (c), Fe Kα (d), and B Kα (e).

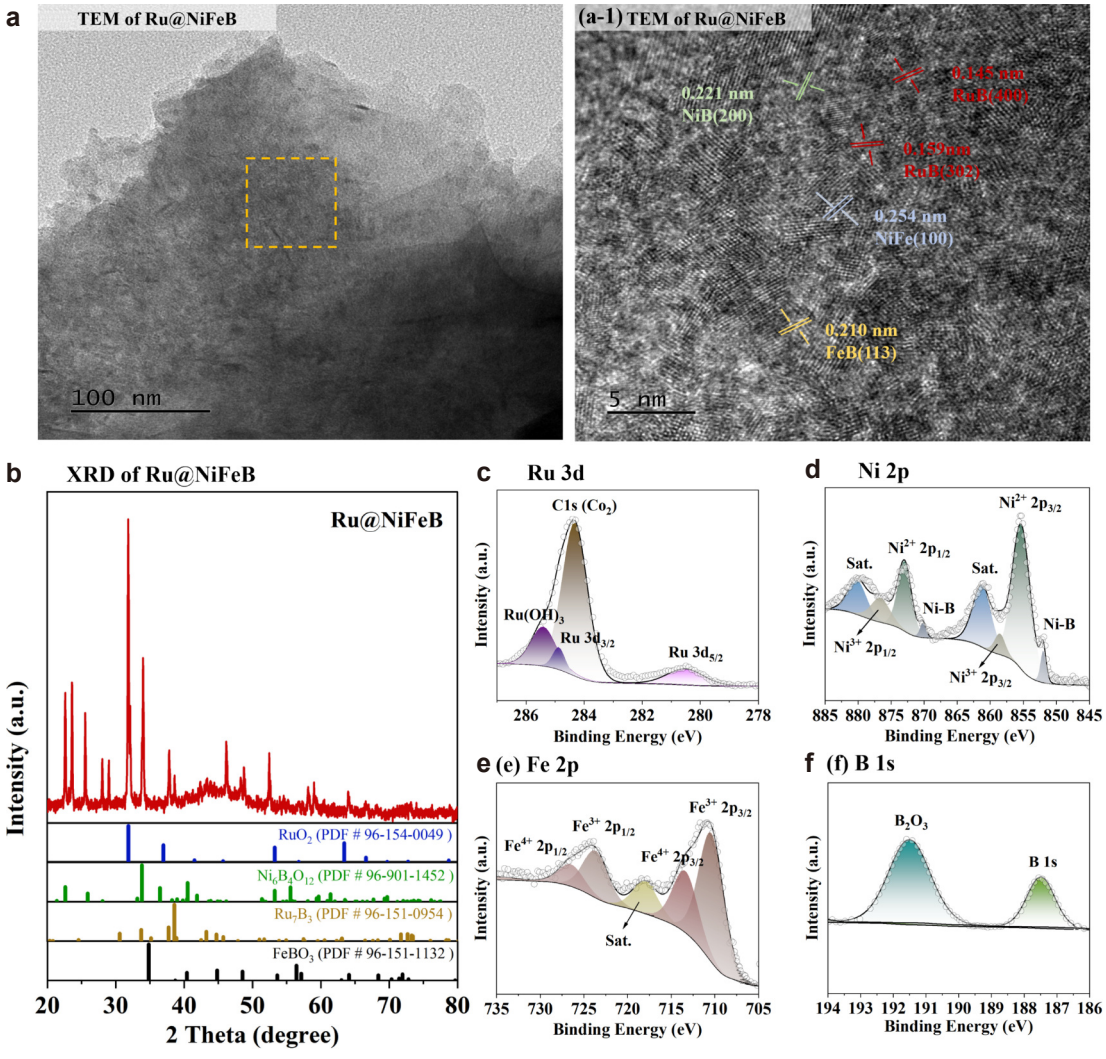

Figure 2 Physical characterization of the optimal Ru@NiFeB electrocatalyst. (a) and (a-1) TEM images and atomic scale analysis of Ru@NiFeB. (b) XRD spectrum of Ru@NiFeB. (c)–(f) XPS spectra of the Ru@NiFeB electrocatalyst.

was conducted on the surface of Ru@NiFeB. As shown in Fig. 2a-1, the lattice spacing of 0.221 nm can be attributed to NiFeB (200). The distances of 0.145 and 0.159 nm correspond to RuB (400) and RuB (302), respectively. The distance of 0.210 nm corresponds to FeB (113). These interplanar spacings indicate a well-defined crystalline structure, characterized by stable interactions among Ru, Ni, Fe, and B, which likely contributing to the catalyst's enhanced electrocatalytic activity. Overall, TEM analysis reveals that the Ru@NiFeB surface comprises numerous small crystallite domains, exhibiting polycrystalline characteristics. This internal structural evolution is expected to play a key role in enhancing the catalyst's electrochemical performance. The XRD spectrum in Fig. 2b provides insight into the crystal structure of the Ru@NiFeB catalyst. Multiple distinct diffraction peaks were observed, with the main peaks at approximately 30°, 45°, 55°, and 65°. These peaks correspond to known compounds, including RuO_2, $Ni_6B_4O_{12}$, Ru_7B_3, and $FeBO_3$, as matched with standard PDF cards (e.g., PDF 96-154-0049, PDF 96-901-1452). Smaller diffraction peaks were observed at 37.55°, 38.81°, 47.62°, 48.21°, and 57.14°. Notably, peaks at approximately 28.5° and 35° correspond to RuO_2, indicating the presence of RuO_2 crystallites in the Ru@NiFeB catalyst. Peaks at approximately 34° and 36° are attributed to $Ni_6B_4O_{12}$, suggesting the preexistence of Ni and B oxides in the NiFeB composite catalyst. Several weaker diffraction peaks at around 38°, 45°, and 50° correspond to Ru_7B_3 and $FeBO_3$, further confirming the chemical bonding and crystalline structure among Ru, Ni, Fe, and B, which is consistent with the TEM analysis.

XPS analysis (Figs. 2c–2f) provides detailed information on the elemental composition and chemical states of the Ru@NiFeB catalyst surface. The full-scan XPS spectrum reveals peaks corresponding to Ru, Ni, Fe, B, C, and O elements, as shown in Fig. S6 in Supplementary Material. Specifically, the binding energies (BEs) of Ru (Ru $3d_{5/2}$), Ni (Ni $2p_{1/2}$), Fe (Fe $2p_{3/2}$), and B (B 1s) were observed at 280.6, 872.9, 713.5, and 187.5 eV, respectively. The characteristic peaks for Ru $3d_{5/2}$, Ni $2p_{1/2}$, Fe $2p_{3/2}$, and B 1s are typically located at 280.0, 873.5, 713.0, and 187.2 eV, respectively[20–22]. In the Ni 2p spectrum, the Ni $2p_{1/2}$ peak shifted by 0.6 eV to a lower binding energy, indicating electron donation to Ni. Similarly, the Ni $2p_{3/2}$ peak also shifted by 0.6 eV to a lower binding energy, further indicating electron acceptance[23]. Ni satellite peaks

were observed at 880.3 and 861.2 eV[20]. The XPS of Fe 2p also exhibits similar trends to those of Ni 2p. The B 1s peak (Fig. 2f) was deconvoluted into two components: B–O (192.6 eV) and B–M (187.2 eV). The presence of B–M bonding confirms electron donation from B to the Ni/Fe d-orbitals, in agreement with previous studies on metal borides[24]. According to Pauling's theory, B has a higher electronegativity (2.04) than Ni (1.91) and Fe (1.93), which facilitates electron donation from B to the metal atoms in NiFeB[23]. The negative shifts in the binding energies of Ni 2p and Fe 2p, along with the positive shifts in B 1s, indicate electron transfer from B to Ni/Fe. This electronic restructuring optimizes the adsorption energies of key OER intermediates (*OH, *O, *OOH), thereby accelerating the rate-determining step and contributing to the low Tafel slope (27 mV/dec) observed in our system. Similar electronic modulation effects have been reported in other Ru-doped transition metal borides[23].

The TEM and XRD analyses indicate that NiFeB exists in a polycrystalline phase, with Ru atoms incorporated as nanoclusters. The Ru $3d_{5/2}$ peak in Fig. 2c shifted by 0.5 eV to a higher binding energy, further supporting electron donation. The Ru $3d_{3/2}$ peak, observed at 284.9 eV, shifted by 0.82 eV from its intrinsic value of 284.08 eV, confirming the successful incorporation of Ru into the NiFeB matrix. These binding energy shifts of the Ru $3d_{5/2}$ and Ru $3d_{3/2}$ peaks indicate enhanced electronic interactions within the NiFeB matrix, which may optimize the electronic structure[24]. The slight shifts in the Ru BEs are likely attributed to lattice strain and charge redistribution[25]. Strong electrostatic interactions are expected to enhance intrinsic activity, improve active-site accessibility, and facilitate the dissociation of H_2O molecules[25]. Furthermore, the peak observed at 285.4 eV corresponds to $Ru(OH)_3$ species, indicating the adsorption of hydroxide ions on the metallic Ru species[26]. The C 1s peak was observed at 284.4 eV and served as the reference for calibration[24].

Raman spectroscopic analysis elucidates the structural evolution of the Ru@NiFeB catalyst OER and its correlation with performance (Fig. S7 in Supplementary Material). Following OER, significant spectral changes emerge: a wide, intense envelope appears in the 400–750 cm^{-1} region, with a band at ~480 cm^{-1} attributable to the Ni–O bending vibration in the γ-NiOOH/NiFeOOH oxyhydroxide, indicating surface reconstruction into an active NiFe (oxy)hydroxide layer[16–18,27]. Critically, distinct Raman modes at ~518 (E_g), ~642 (A_{1g}), and ~702 cm^{-1} (B_{2g}), characteristic of rutile RuO_2, along with bands near ~430 and ~588 cm^{-1} assigned to Ru^{4+} and Ru^{3+} species, are observed[28]. These features, consistent with the faint but identifiable RuO_2 diffraction peaks (PDF #96-154-0049) in XRD, demonstrate the partial oxidation of Ru nanoparticles into crystalline RuO_x domains under anodic potential. In summary, the OER process drives the transformation of the precursor into a composite heterostructure, where highly active RuO_x nanocrystals are embedded within a reconstituted, porous, and robust NiFe hydroxide matrix. This unique architecture synergistically combines the high intrinsic activity of RuO_x sites, which lowers the reaction energy barrier, with the structural stability and abundant triple-phase boundaries provided by the host matrix, thereby accounting for the enhanced OER performance. vided by the host matrix, thereby accounting for the enhanced OER performance.

The XPS analysis further confirms the successful incorporation of Ru into the NiFeB matrix, which is expected to enhance the electrochemical performance of the catalyst. The Ni–B peak (approximately 851.9 eV) provides additional evidence of bonding between Ni and B. Overall, the XPS data suggest that the surface of Ru@NiFeB contains multiple oxidation states of Ru, Ni, Fe, and B, and that interactions among these elements likely contribute to the enhanced catalytic activity and stability of the catalyst.

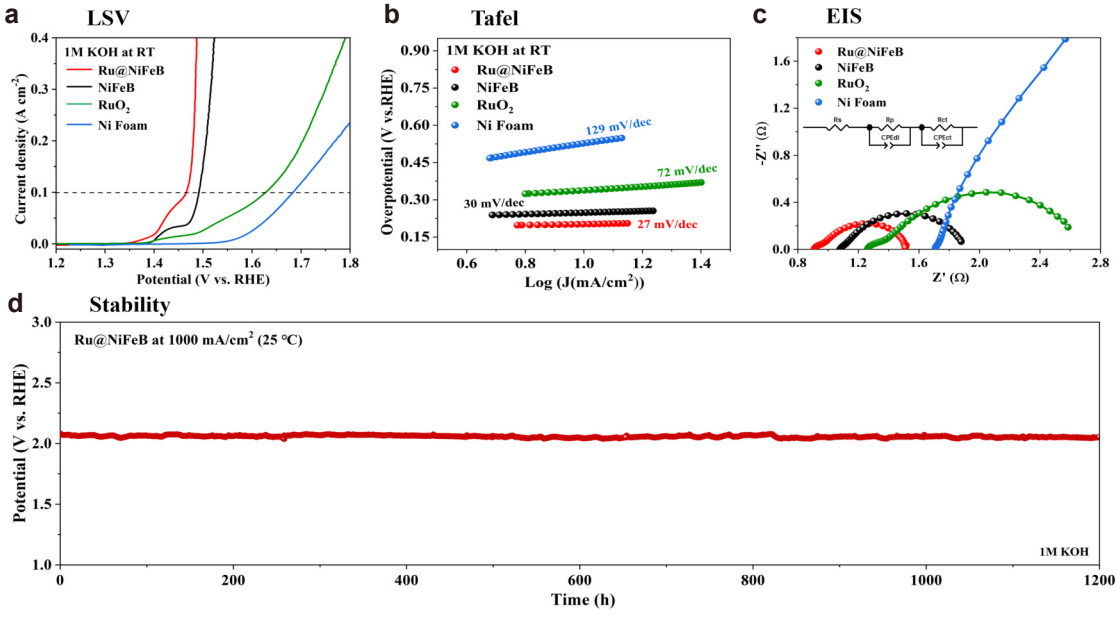

Figure 3 Half-cell electrochemical properties of Ru@NiFeB in 1 mol/L KOH. (a) Half-cell OER LSV curves at room temperature (25°C). (b) Tafel plots and slope values. (c) OER electrochemical impedance spectroscopy (EIS) plots of Ru@NiFeB. (d) Half-cell stability test.

The surface wetting behavior of the Ru@NiFeB electrode was investigated to evaluate its interaction with the aqueous electrolyte. As shown in Video in Supplementary Material, the catalyst exhibits a contact angle of nearly 0°, indicating superhydrophilic characteristics. This extreme wettability is a direct consequence of the hierarchical nanosheet architecture and the hydrophilic nature of the metal (oxy)hydroxide species, which collectively generate capillary forces that promote spontaneous electrolyte permeation. Such a superhydrophilic surface ensures that the entire high-surface-area nanostructure, including interior pores, is fully accessible to the electrolyte, thereby maximizing the utilization of active sites. Furthermore, this property is expected to facilitate rapid detachment of O_2 gas bubbles generated during the OER process, minimizing bubble shielding at high current densities and contributing to the outstanding operational stability observed in subsequent tests.

3.2 Electrochemical OER properties

The linear sweep voltammetry (LSV) polarization curves in Fig. 3a reveal that the Ru@NiFeB electrode achieves an exceptionally low overpotential of 235 mV to reach a current density of 100 mA/cm² in 1 mol/L KOH. All LSV curves were recorded at a scan rate of 5 mV/s in 1 mol/L KOH at room temperature (RT, 25°C). This performance not only significantly surpasses that of undoped NiFeB (261 mV), bare Ni foam (453 mV), and noble-metal RuO_2 (398 mV) electrodes but also ranks among the most active OER electrocatalysts reported to date, as benchmarked in Table S1 in Supplementary Material. Further comparisons reveal that Ru@NiFeB exhibits a lower overpotential and a more stable current response at elevated current densities. Specifically, in the high current-density region, Ru@NiFeB demonstrates faster reaction kinetics than NiFeB, indicating superior resistance to current decay. Under high current-density conditions, the OER performance of Ru@NiFeB is further enhanced, suggesting that the introduction of Ru not only increases the number of active sites but also optimizes the catalyst's electronic structure, thereby improving charge-transfer efficiency.

Tafel analysis, shown in Fig. 3b, reveals that the Tafel slope of Ru@NiFeB is 27 mV/dec, which is lower than that of NiFeB (30 mV/dec), and significantly outperforms both Ni foam (129 mV/dec) and Pt/C (171 mV/dec). The reduced Tafel slope indicates faster interfacial reaction kinetics and a lower activation energy barrier for the OER. This enhancement can be attributed to the introduction of trace Ru species, which effectively promote the reaction rate and facilitate charge transfer, likely by optimizing the adsorption and desorption energetics of key oxygen intermediates. Furthermore, the Ru@NiFeB catalyst exhibits a distinct electronic synergy among Ru, Ni, and Fe sites, fine-tuning the binding behavior of intermediates such as *OH, *O, and *OOH, thereby accelerating the rate-determining step of the OER. Such electronic cooperation contributes to the enhanced electrocatalytic performance and rapid reaction kinetics of Ru@NiFeB, rendering it a highly promising candidate for efficient green hydrogen production.

To further investigate the OER kinetics, Nyquist plots were recorded at 1.5 V vs. RHE, as shown in Fig. 3c. The fitted data extracted from the Nyquist plot reveal that the electrochemical charge-transfer resistance (Rct) of the Ru@NiFeB sample is the smallest at 0.59 Ω, significantly lower than that of NiFeB. This result indicates that Ru doping effectively enhances solid–liquid interfacial conductivity and charge-transfer rate, facilitating the maintenance of a lower polarization resistance at high current densities. Combined with the low overpotential

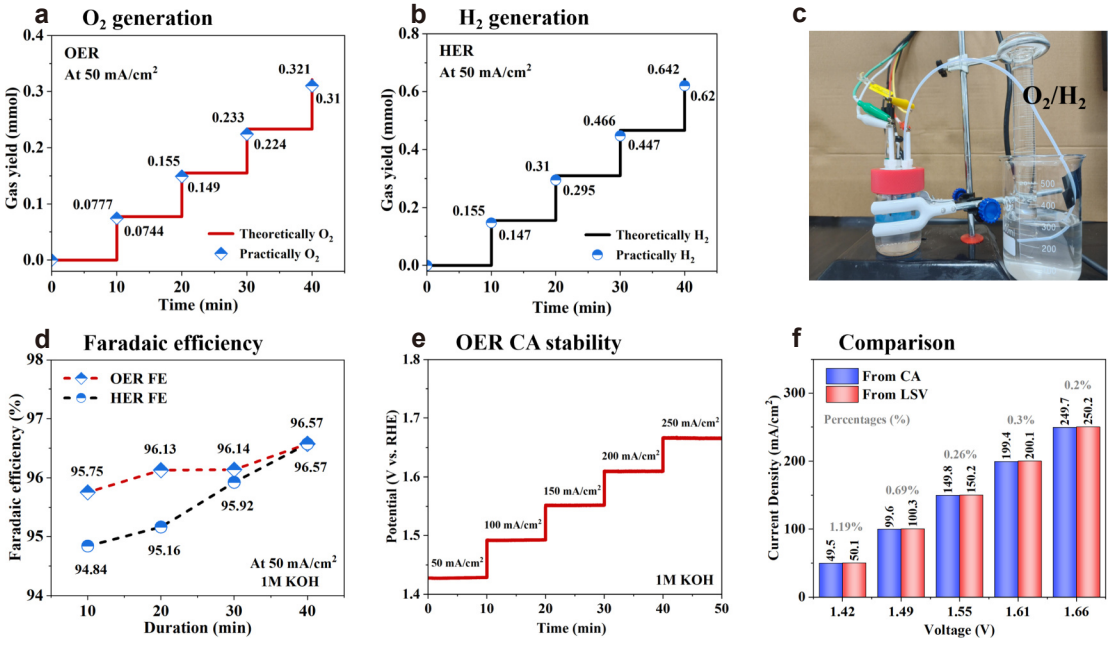

Figure 4 The best Ru@NiFeB FE test in 1 mol/L KOH and steady-state OER chronoamperometry (CA) in 1 mol/L KOH. Actual and theoretical O_2 (a) and H_2 (b) generation in 10–40 min. (c) Digital photograph of water-gas displacement system. (d) FE measurement of the best Ru@NiFeB. (e) OER CA response at different voltages of Ru@NiFeB. (f) Comparison of LSV and CA with the percentage difference between LSV and CA.

from LSV and the small Tafel slope, these analyses collectively corroborate the superior intrinsic kinetics of Ru@NiFeB.

As shown in the Figs. S8a and S8b in Supplementary Material, the electrochemical double-layer capacitance (C_{dl}) and ECSA of the Ru@NiFeB catalyst were determined using cyclic voltammetry in the non-Faradaic region at scan rates ranging from 20 to 100 mV/s, with 20 mV/s increments, between 0.16 and 0.26 V vs. Hg/HgO. Figure S8c in Supplementary Material presents the OER anodic and cathodic currents as a function of scan rate. The measure C_{dl} for Ru@NiFeB was 13.9 mF/cm^2, higher than that of NiFeB. Using the formula ECSA = C_{dl}/C_s, where C_s = 0.04 mF/cm^2, the ECSA of Ru@NiFeB was calculated to be 137.75 cm^2.

The proportionality between C_{dl} and ECSA suggests that a higher C_{dl} value is associated with an increased ECSA, which provides more active sites, facilitates faster interfacial interactions, and reduces the energy barrier for the OER process[29–31]. Compared to bare NiFeB, Ru nanoclusters significantly enhance the ECSA by exposing additional accessible active sites. The Ru@NiFeB catalyst maintains a dense conductive network, while its nanosheet/branch-like architecture ensures sufficient active-site availability and a reduced diffusion distance, thereby improving catalytic efficiency for the OER. The Ru@NiFeB catalyst features a dense conductive network and a hierarchical nanosheet morphology, which together ensure abundant active site exposure and short diffusion paths, thereby enhancing OER efficiency. As shown in Fig. 3d, the half-cell system maintains stable performance over 1000 h at 1000 mA/cm^2 in 1 mol/L KOH, confirming its excellent current stability.

The OER mechanism is as follows:

(i) $M+OH^- \rightarrow M-OH^* + e^-$,

(ii) $M-OH^* + OH^- \rightarrow M-O^* + H_2O + e^-$,

(iii) $M-O^* + OH^- \rightarrow M-OOH^* + e^-$,

(iv) $M-OOH^* + OH^- \rightarrow M + O_2 + H_2O + e^-$,

where M represents the metallic active sites, and M–OH, M–O, and M–OOH are reaction intermediates[32–34]. Steps (iii) and (iv) are considered the rate-determining steps.

The turnover frequency was evaluated to assess the intrinsic activity of the electrocatalyst. After 60 min of reaction, Ru@NiFeB exhibited TOF values of 22.29 per site at an overpotential (η) of 150 mV, indicating superior intrinsic activity and faster O_2 generation rates.

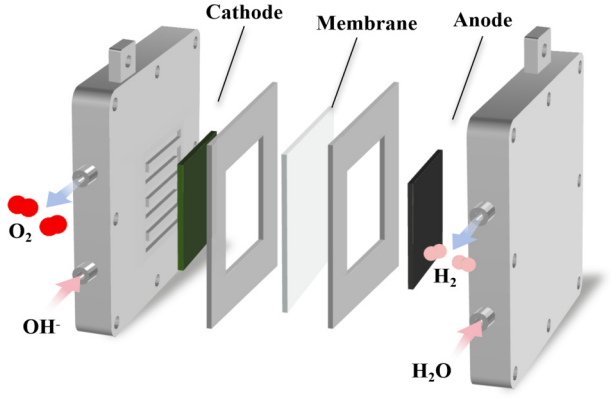

Scheme 2 Full cell component of Ru@NiFeB (+) || Pt/C (–).

Faradaic efficiency (FE), which represents the ratio of experimentally generated H_2 or O_2 to the theoretical amount, is a key parameter for evaluating charge-transfer efficiency in practical applications[35–37]. To investigate FE, electrochemical tests were performed at a current density of 50 mA/cm^2 in 1 mol/L KOH, as shown in Figs. 4a and 4b. The evolved gas was collected via water displacement, as illustrated in Fig. 4c. Ru@NiFeB exhibited FEs of 96.15% for O_2 evolution and 95.62% for H_2 evolution, yielding an overall efficiency of approximately 95.89%. These results indicate minimal side reactions and a high conversion rate. The FE values demonstrate that Ru@NiFeB operates efficiently within practical application ranges, minimizing gas recombination at the electrode surface.

Ru@NiFeB exhibits highly comparable OER performance, rendering it a promising candidate for efficient water splitting. Overall, the Ru@NiFeB catalyst demonstrates superior OER performance in this system. The enhanced performance can be attributed to its well-designed nanosheet morphology, increased surface area, abundant active sites, and high intrinsic activity[24, 35]. The incorporation of Ru into NiFeB optimizes the adsorption and desorption of oxygen intermediates[14,25], adjusts the electronic configuration, and reduces charge-transfer resistance, thereby further enhancing its electrochemical performance.

The steady-state OER CA response of Ru@NiFeB was measured in 1 mol/L KOH. Figures 4e and 4f presents the OER CA response of Ru@NiFeB at different current densities. Figure 4f compares the LSV and CA data, along with the percentage difference between the LSV and CA measurements. During high-current electrolysis, a substantial amount of gas bubbles was generated on the electrode surface. Nevertheless, the current remained stable with minimal deviation, demonstrating that the Ru@NiFeB electrode can sustain steady operation under high-current-density conditions.

3.3 Post-OER characterization

To gain deeper insight into the chemical state evolution and structural stability of the Ru@NiFeB catalyst under operating conditions, we performed detailed post-mortem XPS analysis on the electrode after prolonged OER testing.

Figure S9a in Supplementary Material compares the high-r-resolution Ru 3d and B 1s spectra before and after the OER durability test. In the Ru 3d region, a distinct positive shift of approximately 0.4 eV is observed after OER, with the main peak moving from 280.47 eV to 280.87 eV (vs. C 1s at 284.8 eV). This shift unambiguously indicates the oxidation of Ru species during the anodic reaction, likely transforming the low-valent Ru into higher oxidation states[25,26]. Such electrochemical oxidation is commonly associated with the formation of surface-active phases that catalyze the OER[17]. Crucially, the intensity and shape of the Ru 3d peaks remain largely unchanged, suggesting negligible dissolution or leaching of Ru during the high-current-density operation. ICP-OES analysis further confirms the retention of Ru content (~2.2 wt.%) after OER, suggesting excellent structural integrity. This remarkable stability of the Ru species directly correlates with the outstanding long-term durability demonstrated in

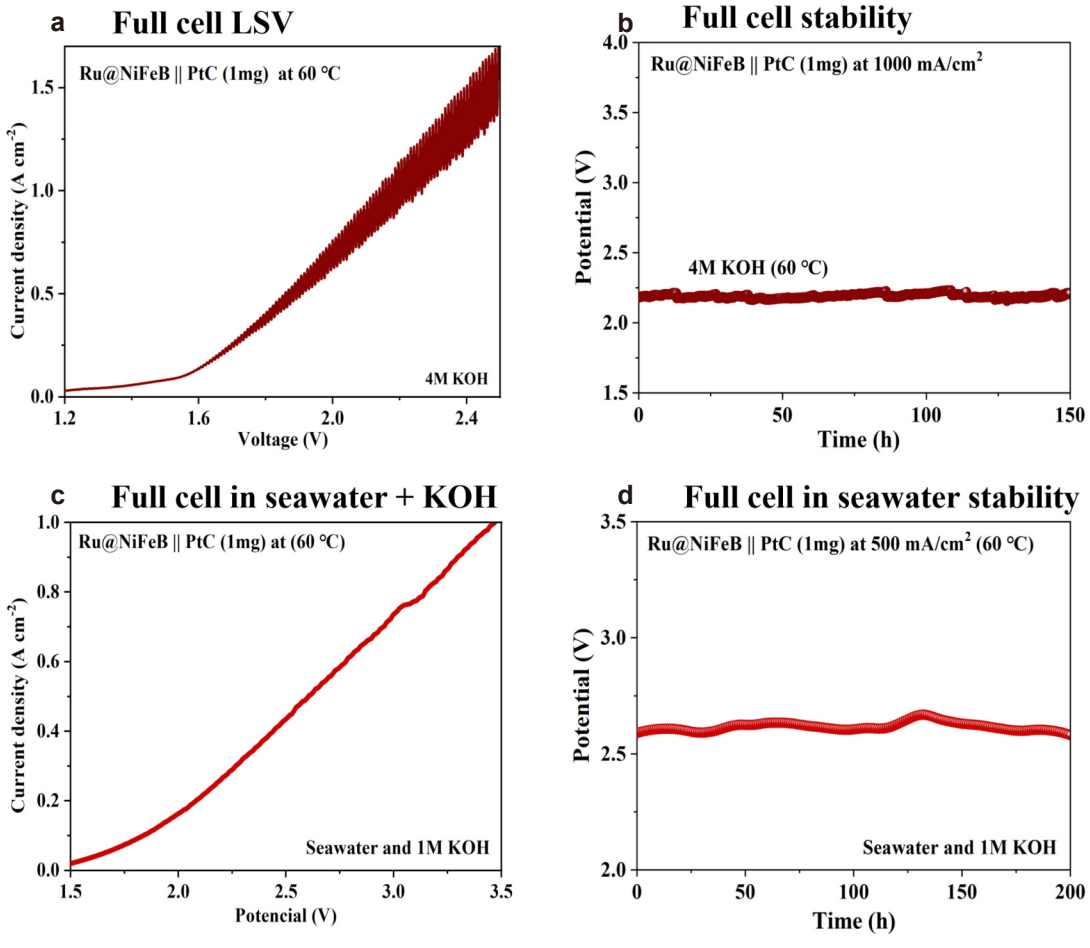

Figure 5 Full-cell activity of Ru@NiFeB under various conditions. (a) Full cell (Ru@NiFeB (+) || Pt/C(−))LSV in 4 mol/L KOH. (b) Full cell stability test in 4 mol/L KOH. (c) Full cell performance in seawater + 1 mol/L KOH. (d) Full cell seawater stability test.

our electrochemical tests.

As shown in Fig. S9b in Supplementary Material, the B undergoes progressive oxidation from B^0 to B^{3+}, accompanied by hydrolysis into $BO_2^-/B(OH)_4^-$ species. This oxidation is reflected in XPS by a decrease in the metal–B peak (~187–189 eV) and a concurrent increase in the B–O peak (~191–193 eV). The electron donation ability of B diminishes as B leaches from the alloy matrix, resulting in a partial shift of metal binding energies toward higher values, which signifies the formation of high-valence Ni^{3+}/Fe^{3+} oxyhydroxides (NiOOH/FeOOH). Simultaneously, the dissolution of B creates abundant defects, vacancies, and porous surface structures, providing additional catalytic sites and accelerating the lattice oxygen-mediated mechanism[32,38]. In the Ru@NiFeB precatalyst, the incorporated boron atoms play a dual role as both "electronic promoters" and "sacrificial activation species". Owing to its relatively low electronegativity, B behaves as an "electron-donating ligand", transferring electron density to neighboring Ru, Ni, and Fe atoms through M–B covalent interactions. This electron donation increases the electron density around the metal centers, stabilizing low-valent metallic states (M^0/M^{2+}) and downshifting the binding energies of corresponding M 2p orbitals. The strengthened metallic bonding and enhanced electronic conductivity facilitate rapid interfacial charge transfer, which is essential for the activation of OER intermediates[39].

3.4 Full-cell performance under industrially relevant conditions

The OWS performance was evaluated in a two-electrode configuration using a zero-gap electrolyzer. A schematic illustration of the custom-built cell assembly, depicting the arrangement of the Ru@NiFeB anode, Pt/C cathode, separator, and electrolyte flow, is presented in Scheme 2[40]. The OWS performance of the Ru@NiFeB electrode was evaluated under industrially relevant conditions. As shown in Fig. 5a, the full cell achieved a low voltage of 2.13 V, delivering a high current density of 1000 mA/cm² in 4 mol/L KOH at 60°C. The fluctuation observed in the LSV curve at high current densities is attributed to the intense generation and detachment of oxygen bubbles, which intermittently affect the electrode–electrolyte contact area. This phenomenon is commonly observed in high-rate water electrolysis and can be mitigated through an optimized electrode architecture[36, 41,42]. This performance can be attributed to the synergistic effect of the catalyst's highly active sites and enhanced intrinsic conductivity. The higher concentration of KOH (K^+ and OH^-) in 4 mol/L KOH reduces solution resistance and facilitates faster ion transport[43]. Moreover, the elevated temperature lowers the activation energy barrier of the electrolysis process[43], favoring more thermodynamically favorable reaction conditions. To gain deeper insight into the charge-trans-

fer dynamics within the practical electrolyzer, EIS was conducted on the full cell. The Nyquist plot in Fig. S10 in Supplementary Material shows an exceptionally low overall impedance of 0.34 Ω for the Ru@NiFeB-based cell, indicating highly efficient charge transport.

Long-term durability under high current density is critical for large-scale hydrogen production. As shown in Fig. 5b, Ru@NiFeB exhibited excellent stability in 4 mol/L KOH at 60°C, maintaining a current density of 1000 mA/cm^2 for over 150 h (more than 6 days) under harsh industrial conditions. These results demonstrate the strong corrosion resistance and mechanical robustness of Ru@NiFeB under high current and prolonged operating conditions.

3.5 Application potential in seawater electrolytes

The viability of the Ru@NiFeB system for hydrogen production from natural resources was evaluated in seawater electrolytes. OWS operations were conducted in both natural seawater and alkaline seawater (seawater + 1 mol/L KOH), as shown in Fig. S11 in Supplementary Material. The Ru@NiFeB system exhibited good stability and performance in natural seawater, achieving a voltage of only 2.60 V at 500 mA/cm^2, as shown in Fig. 5c, indicating excellent performance for natural water electrolysis.

Furthermore, as presented in Table S2 in Supplementary Material, the OWS performance of Ru@NiFeB in seawater + 1 mol/L KOH was compared with recent literature reports. In alkaline seawater, the OWS performance of Ru@NiFeB is comparable to that of advanced electrocatalysts. The excellent OER activity at the anode is a key factor contributing to Ru@NiFeB's outstanding full-cell OWS performance[44].

Typically, the performance in natural seawater is lower than in freshwater due to the presence of various cations and anions, such as Ca^{2+}, Mg^{2+}, F^-, Cl^-, and Br^-, as well as other chemical species, bioelements, and particulate matter, which complicate natural water electrolysis[45]. During electrolysis in natural seawater, the formation of white precipitates was observed, likely corresponding to $Mg(OH)_2$ or/and $Ca(OH)_2$[45]. In alkaline seawater (seawater + 1 mol/L KOH), the Ru@NiFeB system demonstrated long-term stability at 500 mA/cm^2, as shown in Fig. 5d, highlighting its strong resistance to corrosion from additional ions, microorganisms, and other contaminants.

The stable performance in seawater electrolysis suggests that Ru@NiFeB has good resistance to Cl^- corrosion. During the reaction, a boron-containing surface layer may form, acting as a physical barrier that effectively prevents the infiltration and corrosion of Cl^- ions into the catalyst's active sites[46]. Meanwhile, the doping of Ru significantly alters the electronic structure of the NiFe active sites. This electronic modulation not only enhances the kinetics of the OER, allowing the catalyst to operate stably at relatively low overpotentials, but also shifts its thermodynamic profile away from the competitive chlorine evolution reaction window[47]. However, further investigation is needed to fully understand the corrosion resistance mechanism in seawater.

4 Conclusion

In this study, we successfully synthesized Ru@NiFeB as an efficient electrocatalyst for the OER using a hybrid approach that combines electrodeposition, chemical treatment, and scalable hydrothermal methods. The incorporation of Ru into the NiFeB matrix significantly enhanced electronic conductivity, electrochemically active surface area, and intrinsic activity, resulting in excellent OER performance, with a low overpotential of 235 mV at 100 mA/cm^2 in 1 mol/L KOH. The catalyst also demonstrated remarkable stability, maintaining a current density of 1000 mA/cm^2 for over 150 h in 4 mol/L KOH at 60°C.

The Ru@NiFeB catalyst exhibits OER activity and stability that meet the benchmarks for industrial applications, positioning it as a cost-effective and robust anode material for water electrolysis. Its exceptional reaction kinetics and adaptability to various water sources arise from the hierarchical nanosheet structure and favorable electronic synergy induced by the incorporation of Ru. The low Ru loading (2.26 wt.%) enables the Ru@NiFeB catalyst to achieve an excellent balance among activity, stability, and cost, which is crucial for practical industrial applications. The high performance at high current densities and long-term stability make it a promising candidate for large-scale green hydrogen production. Consequently, this work presents a rational design strategy for developing high-performance electrocatalysts for the scalable roduction of green hydrogen.

Acknowledgements

None.

Author contribution statement

Shiyu Chen: Data curation, Conceptualization, Writing-original draft, Methodology; **Yang Li**: Data curation, Investigation; **Chunling Lu**: Supervision, Validation; **Biao Wang**: Supervision, Writing-review & editing; **Junru Jiang**: Data curation, Supervision; **Dongchao Qiu**: Software, Investigation; **Bingbing Niu**: Conceptualization, Resources, Supervision, Project administration, Writing-review & editing; **Tao Feng**: Validation, Methodology, Project administration, Writing-review & editing. All the authors have approved the final manuscript.

Data availability

The data that support the findings of this study are available from the corresponding author upon reasonable request.

Declaration of competing interest

All authors declare no conflicts of interest in this work.

Funding

This work was supported by Natural Science Foundation of China (Grant Nos. W2441008 and 52502266) and Natural Science Foundation of Guangdong Province (Grant No. 2514050000790).

Use of AI statement

None.

Electronic Supplementary Material: Supplementary material is available in the online version of this article at https://doi.org/10.26599/EMD.2026.9370085

References

[1] Wang, X., Liu, F. M., Qin, H. Y., Li, J. H., Chen, X. J., Liu, K. M., Zhao, T. T., Yang, W. L., Yu, M., Fan, G. L., et al. (2024). Electrosynthesis of transition metal coordinated polymers for active and stable oxygen evolution. *Angew. Chem. Int. Ed.* 63, e202409628.

[2] Luo, Y. T., Tang, L., Khan, U., Yu, Q. M., Cheng, H. M., Zou, X. L., Liu, B. L. (2019). Morphology and surface chemistry engineering toward pH-universal catalysts for hydrogen evolution at high current density. *Nat. Commun.* 10, 269.

[3] Zhao, Y. F., Lu, X. F., Wu, Z. P., Pei, Z. H., Luan, D. Y., Lou, X. W. (2023). Supporting trimetallic metal-organic frameworks on S/N-doped carbon macroporous fibers for highly efficient electrocatalytic oxygen evolution. *Adv. Mater.* 35, 2207888.

[4] van der Heijden, O., Park, S., Eggebeen, J. J. J., Koper, M. T. M. (2023). Non-kinetic effects convolute activity and Tafel analysis for the alkaline oxygen evolution reaction on NiFeOOH electrocatalysts. *Angew. Chem. Int. Ed.* 62, e202216477.

[5] Liu, W. X., Zheng, D., Deng, T. Q., Chen, Q. L., Zhu, C. Z., Pei, C. J., Li, H., Wu, F. F., Shi, W. H., Yang, S. W., et al. (2021). Boosting electrocatalytic activity of 3d-block metal (Hydro)oxides by ligand-induced conversion. *Angew. Chem. Int. Ed.* 60, 10614–10619.

[6] Li, X. J., Zhang, H. K., Hu, Q., Zhou, W. L., Shao, J. X., Jiang, X. X., Feng, C., Yang, H. P., He, C. X. (2023). Amorphous NiFe oxide-based nanoreactors for efficient electrocatalytic water oxidation. *Angew. Chem. Int. Ed.* 62, e202300478.

[7] Li, Y. T., Zhang, Y., Shi, R. D., Xu, X. X., Wang, X., Zhou, G. B. (2025). Hollow Fe_2O_3-$NiFe_2O_4$ hetero-nanoframes coupled with N-doped graphene for boosted electrochemical water oxidation through optimizing intermediate bonding. *Chem. Eng. J.* 512, 162666.

[8] Fan, Y. L., Zhang, C. J., Zhang, L. Y., Zhou, J., Li, Y. Z., Huang, Y. C., Ma, J. Y., Chan, T. S., Chen, C. T., Jing, C., et al. (2024). Novel mechanism of Fe^{4+}/Ni^{3+} synergistic effect via exchange energy gain for boosting water oxidation. *Chem Catal.* 4, 100981.

[9] Ding, P. J., Hu, Q., Chai, Z. W., Zhou, H. B., Lu, G. H., Teobaldi, G., Selloni, A., Liu, L. M. (2024). Distribution of high valence Fe sites in nickel–iron hydroxide catalysts for water oxidation. *J. Mater. Chem. A* 12, 2830–2838.

[10] Guo, F., van Ruijven, B. J., Zakeri, B., Zhang, S. N., Chen, X., Liu, C. Y., Yang, F., Krey, V., Riahi, K., Huang, H., et al. (2023). Author Correction: implications of intercontinental renewable electricity trade for energy systems and emissions. *Nat. Energy* 8, 1418–1418.

[11] Chen, Y. W., Guo, J., Chen, B. M. (2025). Oxygen vacancy-induced crystal-amorphous interface in NiFe LDH catalyst for enhanced OER performance. *Surf. Interfaces* 69, 106829.

[12] Zhao, S. L., Tan, C. H., He, C. T., An, P. F., Xie, F., Jiang, S., Zhu, Y. F., Wu, K. H., Zhang, B. W., Li, H. J., et al. (2020). Structural transformation of highly active metal–organic framework electrocatalysts during the oxygen evolution reaction. *Nat. Energy* 5, 881–890.

[13] Yu, M. Q., Budiyanto, E., Tüysüz, H. (2022). Principles of water electrolysis and recent progress in cobalt-, nickel-, and iron-based oxides for the oxygen evolution reaction. *Angew. Chem. Int. Ed.* 61, e202103824.

[14] Zhang, Y. C., Han, C. D., Gao, J., Pan, L., Wu, J. T., Zhu, X. D., Zou, J. J. (2021). NiCo-based electrocatalysts for the alkaline oxygen evolution reaction: a review. *ACS Catal.* 11, 12485–12509.

[15] Gong, M., Li, Y. G., Wang, H. L., Liang, Y. Y., Wu, J. Z., Zhou, J. G., Wang, J., Regier, T., Wei, F., Dai, H. J. (2013). An advanced Ni–Fe layered double hydroxide electrocatalyst for water oxidation. *J. Am. Chem. Soc.* 135, 8452–8455.

[16] Bai, Y. K., Liu, Z. J., Wang, X. X., Zhang, Z. X., Liu, K., Gao, C. B. (2024). Tailoring Ni-Fe-B electronic effects in layered double hydroxides for enhanced oxygen evolution activity. *Small* 20, 2407564.

[17] Habib, M. A., Lin, S. S., Joni, M. H., Dristy, S. A., Mandavkar, R., Jeong, J. H., Lee, J. (2025). Ru/NiMnB spherical cluster pillar for highly proficient green hydrogen electrocatalyst at high current density. *J. Energy Chem.* 100, 397–408.

[18] Lu, B. W., Dun, R., Wang, W., Huang, J., Wu, J. X., Hua, Z. L., Shi, J. L. (2024). Electroless plating synthesis of bifunctional crystalline/amorphous Pd-NiFeB heterostructure catalysts for boosted electrocatalytic water splitting. *Appl. Catal. B: Environ.* 342, 123343.

[19] Aras, F., Burkhardt, U., Ormeci, A., Borrmann, H., Altendorf, S. G., Grin, Y., Antonyshyn, I. (2025). Chemical behavior of Mo_2TMB_2 (*TM* = Fe, Co, Ni) upon the oxygen evolution reaction (OER). *ACS Mater. Au* 5, 718–731.

[20] Chen, N., Che, S., Liu, H. C., Li, G. H., Ta, N., Feng, J. C., Jiang, B., Wu, N., Li, Z. X., Yu, W. Q., et al. (2023). Multistage interfacial engineering of 3D carbonaceous Ni_2P nanospheres/nanoflowers derived from Ni-BTC metal–organic frameworks for overall water splitting. *J. Colloid Interface Sci.* 638, 582–594.

[21] Pal, M., Pal, U., Jiménez, J. M. G. Y., Pérez-Rodríguez, F. (2012). Effects of crystallization and dopant concentration on the emission behavior of TiO_2:Eu nanophosphors. *Nanoscale Res. Lett.* 7, 1.

[22] Schild, D. (2008). X-ray photoelectron spectroscopy. In *Hydrogen Technology: Mobile and Portable Applications*. Léon, A., Ed. Berlin, Heidelberg: Springer, p 575–601.

[23] Tian, R. F., Zhao, S. J., Li, J. K., Chen, Z. B., Peng, W. F., He, Y., Zhang, L. L., Yan, S., Wu, L. L., Ahuja, R., et al. (2021). Pressure-promoted highly-ordered Fe-doped-Ni_2B for effective oxygen evolution reaction and overall water splitting. *J. Mater. Chem. A* 9, 6469–6475.

[24] Gupta, S., Patel, N., Miotello, A., Kothari, D. C. (2015). Cobalt-boride: an efficient and robust electrocatalyst for hydrogen evolution reaction. *J. Power Sources* 279, 620–625.

[25] Wang, Y. J., Wang, J. K., Xie, T. P., Zhu, Q. Y., Zeng, D., Li, R., Zhang, X. D., Liu, S. L. (2019). Ru doping in $Ni(OH)_2$ to accelerate water reduction kinetics for efficient hydrogen evolution reaction. *Appl. Surf. Sci.* 485, 506–512.

[26] Cen, J. M., Shen, P. K., Zeng, Y. F. (2022). Ru doping NiCoP hetero-nanowires with modulated electronic structure for efficient overall water splitting. *J. Colloid Interface Sci.* 610, 213–220.

[27] Wen, J., Tang, S., Ding, X., Yin, Y., Song, F., Yang, X. (2024). In situ Raman study of layered double hydroxide catalysts for water oxidation to hydrogen evolution: Recent progress and future perspectives. *Energies* 17, 5712.

[28] Chen, D., Yu, R., Yu, K., Lu, R., Zhao, H., Jiao, Y., Zhu, J., Wu, J., Mu, S. (2024). Bicontinuous RuO_2 nanoreactors for acidic water oxidation. *Nat. Commun.* 15, 3928.

[29] Habib, M. A., Burse, S., Lin, S. S., Mandavkar, R., Joni, M. H., Jeong, J. H., Lee, S. S., Lee, J. (2024). Dual-functional Ru/Ni-B-P electrocatalyst toward accelerated water electrolysis and high-stability. *Small* 20, 2307533.

[30] Bi, M., Zhang, Y., Jiang, X. H., Sun, J. W., Wang, X., Zhu, J. W., Fu, Y. S. (2024). Ruthenium-induced activation of molybdenum-cobalt phosphide for high-efficiency water splitting. *Adv. Funct. Mater.* 34, 2309330.

[31] Shen, F., Wang, Y. M., Qian, G. F., Chen, W., Jiang, W. J., Luo, L., Yin, S. B. (2020). Bimetallic iron-iridium alloy nanoparticles supported on nickel foam as highly efficient and stable catalyst for overall water splitting at large current density. *Appl. Catal. B: Environ.* 278, 119327.

[32] Wu, F., Tian, F., Li, M., Geng, S., Qiu, L., He, L., Li, L., Chen, Zh., Yu, Y., Yang, W., Hou, Y. (2025). Engineering lattice oxygen regeneration of nife layered double hydroxide enhances oxygen

evolution catalysis durability. *Angew. Chem. Int. Ed.* 64, e202413250.

[33] Ma, G. Y., Ye, J. T., Qin, M. Y., Sun, T. Y., Tan, W. X., Fan, Z. H., Huang, L. F., Xin, X. (2023). Mn-doped NiCoP nanopin arrays as high-performance bifunctional electrocatalysts for sustainable hydrogen production via overall water splitting. *Nano Energy* 115, 108679.

[34] Jung, S., Senthil, R. A., Min, A., Kumar, A., Moon, C. J., Jeong, G. H., Kim, T. W., Choi, M. Y. (2024). Exploring Ir-doped NiFe-LDH nanosheets *via* a pulsed laser for oxygen evolution kinetics: *in situ* Raman and DFT insights. *J. Mater. Chem. A* 12, 8694–8706.

[35] Tiwari, J. N., Dang, N. K., Sultan, S., Thangavel, P., Jeong, H. Y., Kim, K. S. (2020). Multi-heteroatom-doped carbon from waste-yeast biomass for sustained water splitting. *Nat. Sustain.* 3, 556–563.

[36] Han, S., Kim, S., Cho, H. J., Lee, J. Y., Ryu, J., Yoon, J. (2025). Dynamic polarization control of Ni electrodes for sustainable and scalable water electrolysis under alkaline conditions. *Nat. Commun.* 16, 4803.

[37] Li, S. J., Luo, W., Gao, Q., Shen, W., Jiang, Y. M., He, R. X., Su, W., Li, M. (2023). Strong electronic coupling induced by synergy of dopant and interface in Ru-Ni_3S_2/Ni_xP_y to boost efficient water splitting. *Appl. Surf. Sci.* 637, 157940.

[38] Pan, Z., Tang, Z., Sun, D., Zhan, Y. (2022). Hierarchical NiCo2S4@NiMoO4 nanotube arrays on nickel foam as an advanced bifunctional electrocatalyst for efficient overall water splitting. *Electrochimica Acta.* 436, 141393.

[39] Wang, N., Xu, A., Ou, P., Hung, S-F., Ozden, A., Lu, Y-R., Abed, J., Wang, Z., Yan, Y., Sun, M-J., et al. (2021). Boride-derived oxygen-evolution catalysts. *Nat. Commun.* 12, 6089.

[40] Mao, J., Iocozzia, J., Huang, J., Meng, K., Lai, Y., Lin, Z. (2018). Graphene aerogels for efficient energy storage and conversion. *Energy Environ. Sci.* 11, 772–799.

[41] Wang, K., Gadea, E. D., Money, B. R., Sirkin, Y. A. P., Scherlis, D.A., Molinero, V. (2025). Nanoparticle electrodes trigger bubble detachment and enhance gas evolution efficiency. *ACS Nano* 19, 16665–16674.

[42] Zeradjanin, A. R., Narangoda, P., Spanos, I., Masa, J., Schlögl, R. (2021). How to minimise destabilising effect of gas bubbles on water splitting electrocatalysts?. *Curr. Opinion Electrochem.* 30, 100797.

[43] Li, S. S., Li, E. Z., An, X. W., Hao, X. G., Jiang, Z. Q., Guan, G. Q. (2021). Transition metal-based catalysts for electrochemical water splitting at high current density: current status and perspectives. *Nanoscale* 13, 12788–12817.

[44] Cao, D., Huang, X. Y., Zhang, H. M., Liu, W. H., Cheng, D. J. (2023). Constructing porous RuCu nanotubes with highly efficient alloy phase for water splitting in different pH conditions. *Chem. Eng. J.* 456, 141148.

[45] Mohammed-Ibrahim, J., Moussab, H. (2020). Recent advances on hydrogen production through seawater electrolysis. *Mater. Sci. Energy Technol.* 3, 780–807.

[46] Li, J., Liu, Y., Chen, H., Zhang, Z., Zou, X. (2021). Design of a multilayered oxygen-evolution electrode with high catalytic activity and corrosion resistance for saline water splitting. *Adv. Func. Mater.* 31, 2101820.

[47] Chen, H., Gao, R-T., Chen, H., Yang, Y., Wu, L., Wang, L. (2024). Ruthenium and silver synergetic regulation NiFe LDH boosting long-duration industrial seawater electrolysis. *Adv. Func. Mater.* 34, 2315674.